14th International Symposium on Turbulence and Shear Flow Phenomena (TSFP14)
Heidelberg, Germany, July 28–31, 2026

NON-EQUILIBRIUM SCALINGS AND STRUCTURES IN THE SPHEROID TURBULENT WAKE

Clement Barbet-Lavergne
Laboratoire de Mecanique des Fluides de Lille
– Kampé de Fériet, LMFL CNRS UMR 9014
Blv Paul Langevin 59655 Villeneuve d'Ascq, France
clement.barbet@centralelille.fr

Pierre Braganca
Laboratoire de Mecanique des Fluides de Lille
– Kampé de Fériet, LMFL CNRS UMR 9014
Blv Paul Langevin 59655 Villeneuve d'Ascq, France
pierre.braganca@centralelille.fr

Christophe Cuvier
Laboratoire de Mecanique des Fluides de Lille
– Kampé de Fériet, LMFL CNRS UMR 9014
Blv Paul Langevin 59655 Villeneuve d'Ascq, France
christophe.cuvier@centralelille.fr

Sutanu Sarkar
Mechanical and Aerospace Engineering
University of California San Diego
La Jolla, California 92093, USA
ssarkar@ucsd.edu

John Christos Vassilicos
Laboratoire de Mecanique des Fluides de Lille
– Kampé de Fériet, LMFL CNRS UMR 9014
Blv Paul Langevin 59655 Villeneuve d'Ascq, France
john-christos.vassilicos@centralelille.fr

INTRODUCTION

The theory of self-preserving axisymmetric turbulent wakes is based on conservation of momentum and turbulent kinetic energy as well as a turbulence dissipation scaling, see Townsend (1976). A non-equilibrium turbulence dissipation scaling has been discovered over the past 15 years in various turbulent flows including turbulent bluff body wakes, see for example work by Dairay *et al.* (2015). The streamwise decay of the mean flow deficit and the streamwise growth of the wake width are different with this non-equilibrium scaling than with the Kolmogorov-equilibrium turbulence dissipation scaling.

Recent simulation results for wakes of slender spheroids rather than bluff bodies suggest the existence of a non-equilibrium dissipation scaling that differs from the one reported till now for various turbulent flows Ortiz-Tarin *et al.* (2021). The wake's mean flow evolution observed in these simulations is consistent with this new non-equilibrium turbulence dissipation scaling, in agreement with the theory of self-preserving wakes.

Our study reports hot-wire anemometry and Stereo-PIV wind-tunnel measurements of the turbulent wake of a $D = 0.160m$ diameter spheroid with 1:6 aspect ratio. We experiment with two different trip sizes for the boundary layer on the spheroid and three values of the global Reynolds number Re_G (defined in terms of the incoming laminar flow's constant inlet velocity U_∞ and the spheroid's diameter D). Non-equilibrium dissipation scalings appear only at our highest Re_G, $Re_G = 10^5$, which is also the Reynolds number where the signature of a large scale coherent structure appears as a localised low-frequency peak in the energy spectrum at a Strouhal number $St = 0.21$. Depending on the trip size, the wake's mean flow evolution is consistent with one or the other non-equilibrium dissipation scaling. At our two lower values of Re_G the turbulence dissipation scaling is classical and there is no low frequency peak in the spectra.

SCALINGS IN AXISYMMETRIC WAKES

The classical, Kolmogorov equilibrium's, turbulence dissipation scaling is $\varepsilon = C_\varepsilon \frac{\mathscr{K}^{3/2}}{\mathscr{L}}$ where ε is the turbulence dissipation rate, $\mathscr{K}$ is the turbulent energy, $\mathscr{L}$ is a measure of the largest turbulent eddies in the flow and the dimensionless coefficient C_ε is independent of inlet conditions and position in the flow. It is obtained from Kolmogorov equilibrium in the inertial range for stationary homogeneous turbulence where there is ample evidence that it is valid. However the turbulence produced in axisymmetric wakes is not homogeneous.

For non-homogeneous turbulent flows, there are regions where a different dissipation scaling law holds, see Vassilicos (2015), and axisymmetric wakes are examples of such flows. This non-equilibrium scaling of dissipation is expressed as a dependence of C_ε on the global Reynolds number Re_G and a local Reynolds number such as the Taylor length-based Reynolds number Re_λ or $Re_\delta \equiv \frac{\sqrt{\mathscr{K}}\delta}{\nu}$ where δ is the wake width and ν is the kinematic viscosity. Note that δ is a local length scale that grows with streamwise distance from the spheroid. Generally, the non-equilibrium dissipation scaling is $C_\varepsilon \sim \frac{\varepsilon \cdot \delta}{\mathscr{K}^{3/2}} \sim (\frac{Re_G}{Re_\delta})^n$. The classical equilibrium case is retrieved for $n = 0$.

According to the theory of self-preserving axisymmetric wakes, the mean flow profile deficit u_0 and half-width δ evolve following power laws which depend on the dissipation exponent n:

$$\frac{u_0}{U_\infty}(x/D) = A \cdot (\frac{x-x_0}{D})^{-2\frac{n+1}{n+3}},$$
$$\frac{\delta}{D}(x/D) = B \cdot (\frac{x-x_0}{D})^{\frac{n+1}{n+3}}.$$

The classical scalings in various textbooks (e.g. Townsend (1976)) follow from $n = 0$. The scalings predicted for and observed in turbulent wakes of bluff bodies over streamwise distances of about 5 to 50 bluff body sizes follow from $n = 1$ (e.g. Dairay *et al.* (2015)). The scalings corresponding to $n = 2$ have been observed in the slender body wake simulations of Ortiz-Tarin *et al.* (2021) at $Re_G = 10^5$.

EXPERIMENTAL APPROACH

The spheroid model used in the experiments has a maximum diameter $D = 0.16$ m making it 0.96 m long, for an aspect ratio of 6:1. Our global Reynolds number values are estimated using this maximum diameter D and stable inflow velocity U_∞. For $D = 0.16$ m, our flows' global Reynolds numbers are $Re_G \approx 5.0 \cdot 10^4$, $7.5 \cdot 10^4$ and 10^5 respectively. The spheroid was placed in the wind tunnel without pitch or yaw angle with $\pm 0.1^\circ$ precision.

Trying to respect the geometry used in Ortiz-Tarin *et al.* (2021), we included an axisymmetric tripping device near the upstream edge of the spheroid model. It consists of a sudden rise of height $T_1 = 0.3$ mm (around 15 wall units typically) in the radial direction at a distance $0.5D$ away from upstream edge. This trip step was used at all Reynolds numbers. One last flow was tested using a step twice as high, $T_2 = 0.6$ mm.

A correct assessment of the average turbulence dissipation rate ε is required, especialy at the centreline of the wake. For this, we use hot-wire anemometry (HWA) and a local isotropy hypothesis on the geometric centreline. This hypothesis has been shown to accurately estimate the true value of ε in other axisymmetric wakes by Direct Numerical Simulations, e.g. Dairay & Vassilicos (2016). We therefore use expression $\varepsilon \approx \varepsilon_{iso} = 15\nu \int_{k_-}^{k_+} k^2 E_x(k) dk$ which requires a well converged power density spectrum $E_x(k)$ of the streamwise velocity fluctuations, where wavenumbers k are obtained from frequencies by Taylor's frozen turbulence hypothesis.

Low frequency stereoscopic particle image velocimetry measurements with a large transverse field of view (SPIV) recordings allow analysis of all three velocity components obtained at each 2D transverse plane. Transverse plane statistics are then used to perform azimuthal averages and obtain radial profiles at all streamwise stations after also averaging over time. With the low frequency acquisition, 10,000 fields can be recorded for each global Reynolds number, tripping and streamwise station, thereby ensuring good statistical convergence for all our statistics.

Thus, we carried out HWA and SPIV. Both methods were used at 12 streamwise locations between $x = 7D$ and $x = 40D$. The HWA measurements were performed using a single wire probe of type 55P11 by Dantec. Those measurements were located both at the centerline ($r = y = z = 0$) and at off-center points ($r = y = 0.5D, z = 0$).

APPARATUS AND PROCEDURES

Our HWA measurement system was mounted on a tripped NACA mast to reduce vibrations. The sensor in all measurements campaigns was a single 55P11 model wire built by Dantec Dynamics. Its main dimensions are 1.25 mm of length with a thickness of 5 μm. Results presented here were obtained with a Dantec streamline bridge system with an inbuilt signal conditioner. Before using Taylor's hypothesis, the signal coming from the anemometer was compensated and amplified with the inbuilt signal conditioner to enhance the signal to noise ratio which is typically of the order of 45 dB for all measurements. The conditioned signal was low-pass filtered at 30 kHz to avoid aliasing and obtained using a sampling frequency adjusted to 50 kHz. We used an overheat ratio of 1.7. The hot wire was calibrated at the beginning and at the end of each measurement at each streamwise location using a King's law fit for constant temperature anemometry.

The PIV system used for the measurements analysed in this paper is represented by the schematic in figure 1. The seeded particles are on average 1 μm in diameter, formed from a glycol and water mixture in a smoke machine.

The particles are illuminated using a low-speed Innolas spitlight 400 compact laser which outputs 150 mJ of light per pulse at 532 nm wavelength and the beam's Rayleigh length exceeds 250 mm.

As no backflow is expected, we separated the light-sheet in two planes 2.7 mm apart, allowing for a high dynamic range which helps augment the captured displacement in this low turbulence intensity flow (Foucaut *et al.* (2014)). This light sheet separation is pictured in the sub-schematic of figure 1.

The imaging system consists of two systems of two sCMOS imager cameras built by LaVision. Each camera has 5.5 megapixel resolution and is fitted with a macro Nikkor 105 mm objective lense (with an f-number set at $f_\# = 8$, obtaining pixel size of 6.5 μm). For each pair, the 2 cameras are placed at the same angle $\Theta = 40.7^\circ$ relative to the illuminated plane. Each pair records a field of view corresponding to half the final combined field. The final field is around $400 \cdot 400$ mm^2. The camera system can be moved as a single entity in the x direction so as to record measurements at different x/D positions.

The PIV images are cross-correlated using an in-house software developed at the LMFL which uses multi-pass (Willert & Gharib (1991)), multi-grid (Soria (1996)) and image deformation features (Scarano (2002)) and (Lecordier & Trinité (2004)). The Soloff reconstruction method is used (Soloff *et al.* (1997)) to obtain the three components of velocity from two cameras. To account for misalignment between the light sheet and the calibration plane, the self-calibration correction method (Coudert & Schon (2001)) and (Wieneke (2005)) is also used in our SPIV processing. The analysis uses 4 passes with final size $24px \cdot 24px$, which roughly implies a 2.8 mm^2 interrogation window size. At the end of this procedure, we have 3-components of the velocity recorded with this resolution at a frequency of 10 Hz.

The azimuthal average of all statistics is performed around the geometric axis of symmetry of the object (i.e. the x axis) which coincides with the geometric center of the wind-tunnel test section, within errors. Note that the azimuthal averaging masks deviations from axial symmetry which are actually present in time-averaged quantities.

Our statistics, e.g. $\langle u_i \rangle$ (where the $i = 1,2,3$ represents the 3 components of fluid velocity vector u_x, u_r, u_φ) are averaged over time and azimuthal angle. The profile $U_x(x,r) \equiv \langle u_1 \rangle(x,r) \equiv \langle u_x \rangle(x,r)$ as a function of distance r from the geometric centreline in the 2D cross-plane at every streamwise location x gives access to the mean flow deficit $u_0(x)$ on the centreline where $r = 0$. By taking the half-width-at-half-depth, i.e. the value of r where $U_\infty - U_x(x,r)$ equals $u_0/2$, we also access $\delta(x)$. Furthermore, the SPIV's 3-component information allows calculations of the time and azimuthaly averaged

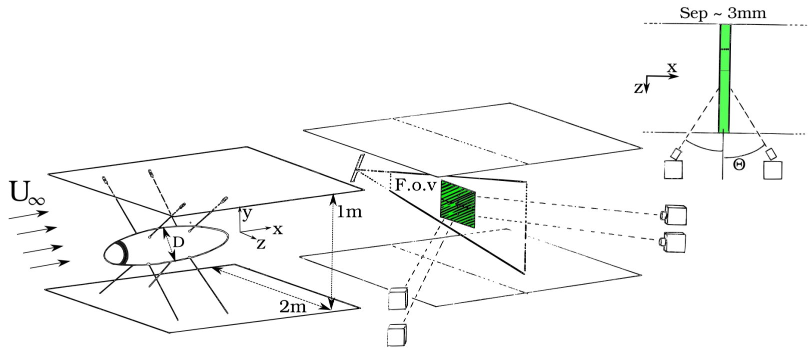

Figure 1: Schematic view of wind tunnel measurements using a SPIV setup with a large field of view (FOV). The schematic is not to scale. The spheroid of maximum thickness D is placed with its axis of symmetry parallel to the laminar inflow which has uniform U_∞ velocity. The spheroid is held by 8 wires which are 0.2 mm thick and can support 17kg of tension. The blockage of the wind tunnel's rectangular section by the spheroid is around 1% at diameter $D = 160$ mm. The cartesian coordinate system, shown in terms of directios, has its origin at the geometric centre of the spheroid volume. Four sCMOS cameras are represented at an angle $\Theta \approx 40.7°$ from the field of view. The SPIV field of view (FOV) is maintained centred at the geometric centre of the wind tunnel section.

TKE $\mathscr{K}(x,r)$ and Reynolds stresses $\langle u_i'u_j'\rangle(x,r)$. $\mathscr{K}_0(x)$ and $\mathscr{R}_0(x)$ are, respectively, the maximum values of $\mathscr{K}(x,r)$ and $|\langle u_i'u_j'\rangle|(x,r)$ along r.

The 3-component fields obtained from our SPIV cannot be used to estimate the average turbulence dissipation rate because our SPIV's spatial resolution is not sufficient given that the interrogation window size is invariably higher than $5\eta_K$ (η_K is the Kolmogorov length). To estimate average turbulence dissipation rates we therefore take single-component HWA measurements on the centerline of our four turblent wakes.

Our spatial resolution l_w/η_K (where l_w is the length of the wire and $\eta_K \equiv (\nu^3/\varepsilon)^{1/4}$) ranges between 2 and 5 for all the measurements. The estimated frequency response of this anemometry system is 1.5 to 5 times higher than $U_x/2\pi\eta$ where U_x is the mean streamwise velocity at the point of measurement. The spatially varying longitudinal velocity component in the direction of the mean flow was recovered from the time-varying velocity measured with the hot wire probe by means of Taylor's frozen turbulence hypothesis (Taylor (1938)). The minimum wavenumber $k_- \approx 1\ m^{-1}$ was chosen so as to have 20 continuous measurements of 120 seconds each for statistical convergence. Power density spectra were computed using the Welch algorithm (Welch, 1967), with $N_{FFT} = 50000$ (number of points used in the Fast Fourier Transform computed for each windowed segment) and an overlap of 75%. The maximum accessible wavenumber is contingent on the effective removal of electronic noise present in the signal. An exponential fit is applied to smooth the spectrum at the high wavenumber viscous range of the spectrum (see pp.233 in Pope (2000)) and $k_+\eta_K \approx 1.0$. The uncertainties in the estimation of the dissipation rate due to this removal of electronic noise occurring at high frequencies are estimated to be lower than 5% for all our measurements. Statistical errors on the estimation of the root mean square fluctuating streamwise velocity u_{rms} in the HWA signals are negligible.

The main quantity estimated using ε is the normalised dissipation rate C_ε. It is estimated using expression $C_\varepsilon = \frac{\delta\cdot\varepsilon}{\mathscr{K}_0^{3/2}}$ which combines the TKE value on the geometric centreline with the centreline turbulence dissipation rate and δ as an estimate of the size of the largest turbulent eddies. (This largest eddy size is often estimated in terms of an integral length $\mathscr{L}$ and it has been shown that $\delta \sim \mathscr{L}$ in various turbulent jets and bluff body wakes, e.g. see Cafiero *et al.* (2020). We used our HWA signals to compute auto-correlation functions $R_{xx}(\tau)$ of $u_x'(t)$, but found that $R_{xx}(\tau)$ does not always reach or cross zero at large enough τ in our spheroid body wakes.)

RESULTS

In all four spheroid wakes tested here, satisfactory self-similarity is achieved from $x/D = 7.0$ to $x/D = 40.1$ for the azimuthally and time averaged radial profiles of the streamwise mean flow velocity $\langle u_x\rangle(r) \equiv U_x(r)$, the TKE $\langle\mathscr{K}\rangle(r)$ and the dominant Reynolds shear stress $\langle u_x'u_r'\rangle(r)$.

Re_G	Trip	α	β	n	x_0/D	St_{peak}
50 000	T_1	-0.69	0.32	0	3.31	N/A
75 000	T_1	-0.65	0.29	0	4.19	N/A
100 000	T_1	-0.97	0.49	1	2.31	0.21
100 000	T_2	-1.21	0.62	2	-1.44	0.21

Table 1: Summary of scaling exponents and virtual origins obtained in the present study for each configuration of the spheroid wake. Values of $St = \frac{f\cdot D}{U_x}$ at the low-frequency peak in the off-centre power density spectra are given as well for the two configurations where such a peak is clearly present. The exponents were extracted using PIV measurements of azimuthaly averaged velocity statistics. The exponents α,β and virtual origin x_0 result from best fits under the constraint (imposed by theory) that x_0 is the same for u_0 and δ. The exponent n is obtained from an independant best fit of $C_\varepsilon \cdot Re_\delta^n$.

The turbulent wake generated at $Re_G = 5.0\cdot 10^4$ by the spheroid with the T_1 trip has scalings $u_0/U_\infty \sim (x-x_0/D)^{-2/3}$ (see figure 3a) and $\delta/D \sim (x-x_0/D)^{1/3}$ (see figure 2a). These

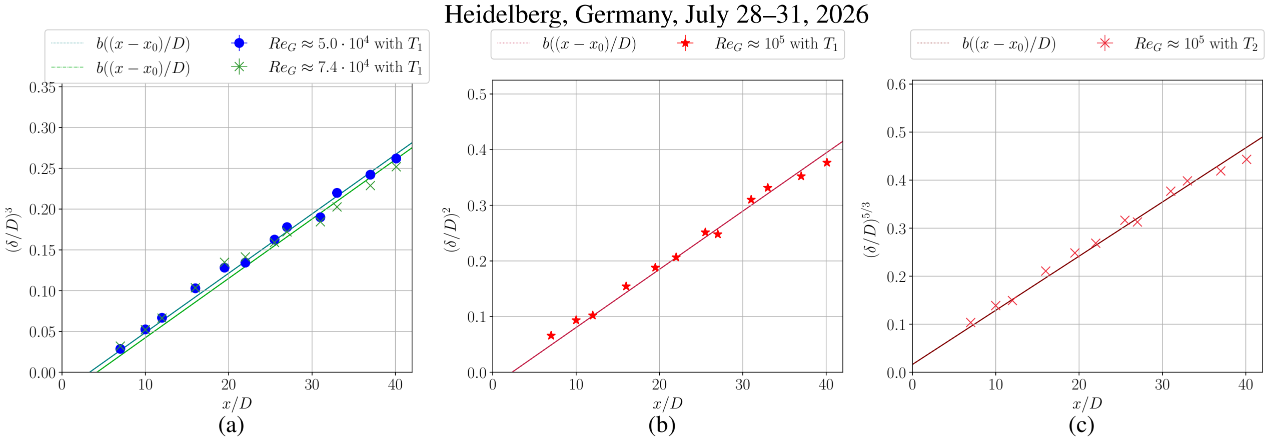

Figure 2: Normalised wake mean flow half-width δ/D scalings obtained by SPIV for each flow. Subfig. 2a : $Re_G = 5.0 \cdot 10^4$ and $Re_G = 7.5 \cdot 10^4$ with classical ($n = 0$) scaling premultiplication to demonstrate linear downstream evolution. Linear fit includes virtual origin and slope $b \approx 0.01$ in all cases. Subfig. 2b : $Re_G = 10^5$ with $n = 1$ non-equilibrium scaling premultiplication. Subfig. 2c : T_2 tripping step at $Re_G = 10^5$ with $n = 2$ non-equilibrium scaling premultiplication.

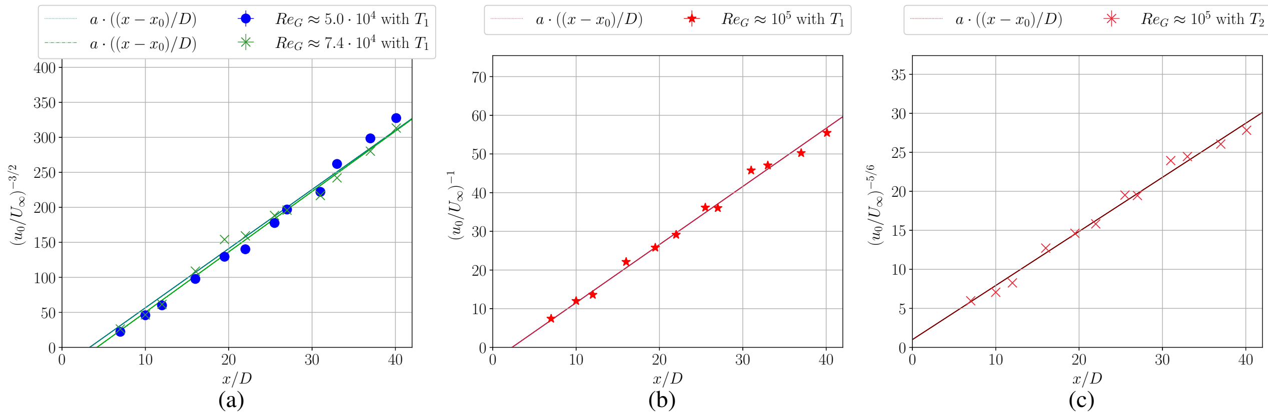

Figure 3: Normalised wake mean flow deficit u_0/U_∞ scalings obtained by SPIV for each flow. Subfig. 3a : $Re_G = 5.0 \cdot 10^4$ and $Re_G = 7.5 \cdot 10^4$ with classical ($n = 0$) scaling premultiplication to demonstrate linear downstream evolution. Linear fit have slopes $a = 8.6$ and $a = 9.51$ respectively. Subfig. 3b : $Re_G = 10^5$ with $n = 1$ non-equilibrium scaling premultiplication, with fitted $a = 1.6$. Subfig. 3c : Large tripping step at $Re_G = 10^5$ with $n = 2$ non-equilibrium scaling premultiplication, with fitted $a = 0.75$.

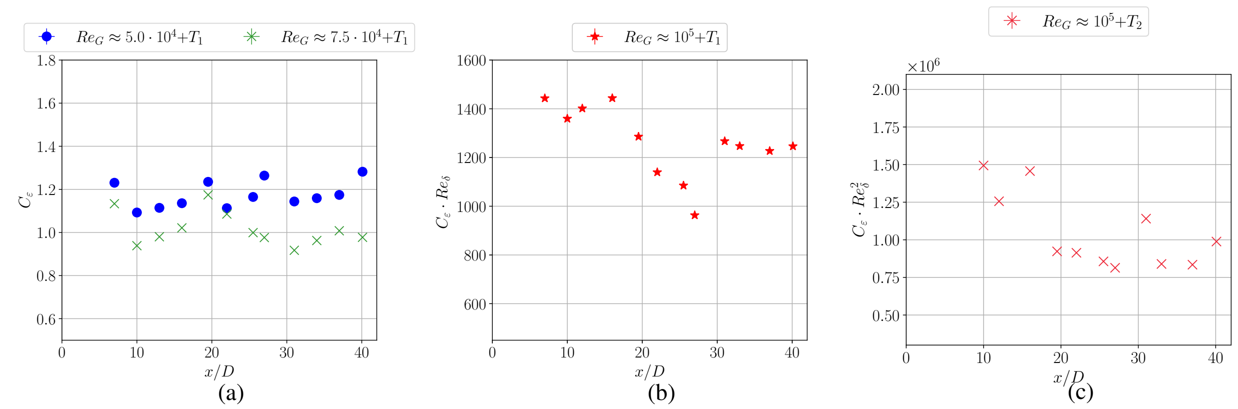

Figure 4: Results for $C_\varepsilon(x/D)$ in Subfig. 4a : $Re_G = 5.0 \cdot 10^4$ and $Re_G = 7.5 \cdot 10^4$. Results for $(Re_\delta \cdot C_\varepsilon)(x/D)$ in Subfig. 4b for $Re_G = 10^5$. For Subfig. 4c we show results for $(Re_\delta^2 \cdot C_\varepsilon)(x/D)$ using larger tripping step T_2 at $Re_G = 10^5$.

exponents $\alpha = -2/3$, $\beta = 1/3$ are consistent as they are expected by the theory for $n = 0$. We can also report the centreline dissipation scaling laws obtained by HWA. For $Re_G = 5.0 \cdot 10^4 + T_1$, we find that $\varepsilon_0 \sim (x - x_0/D)^{-2.3}$, which follows for $n = 0$ also. The dissipation coefficient's exponent $n = 0$ therefore accounts for the values of exponents α, β in the $Re_G = 5.0 \cdot 10^4 + T_1$ case. This means that C_ε should take the same value at different positions on the centreline, i.e. it should be independent of x. In fact, we find $C_\varepsilon \approx 1.2 \pm 0.1$ in figure 4a.

The scalings of u_0 and δ are the same for the turbulent wake generated at $Re_G = 7.5 \cdot 10^4$ by the spheroid with the

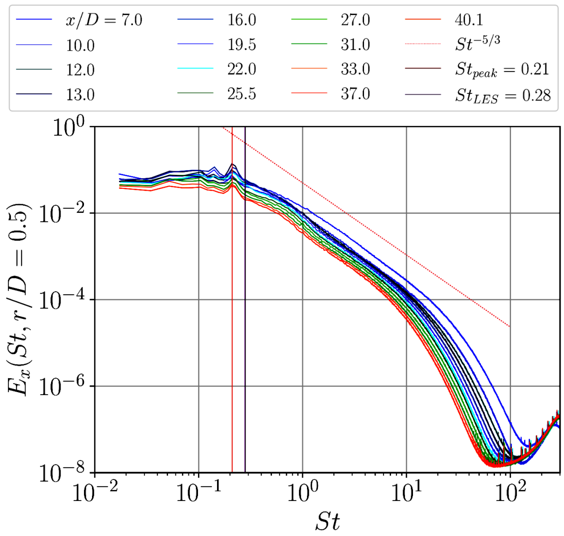

Figure 5: HWA measured power spectral densities (energy spectra) $E_x(St, r = 0.5D)$ of streamwise velocity fluctuations off the centerline showing an inertial range with an approximate $-5/3$ power law spectrum in most streamwise positions of all four configurations. The Reynolds number is $Re_G = 10^5$ with T_1 trip size. At this highest Reynolds number we observe a clear peak at frequency $St = \frac{f \cdot D}{U_x} \approx 0.21$.

T_1 trip: $u_0/U_\infty \sim (x - x_0/D)^{-2/3}$ (figure 3a) and $\delta/D \sim (x - x_0/D)^{1/3}$ (figure 2a). Furthermore, we show with figure 4a that C_ε is also close to 1 and approximately constant with x ($n = 0$) in agreement with the observed $\alpha = -2/3$ and $\beta = 1/3$. Given the overall agreement with and closeness to $n = 0$ behaviour, we conclude that, in the region $x/D = 7.0$ to $x/D = 40.1$, the turbulent wake of the 6:1 spheroid with T1 trip has classical wake scalings corresponding to the $n = 0$ solution when $Re_G = 5.0 \cdot 10^4$ and $Re_G = 7.5 \cdot 10^4$.

As the global Reynolds number is increased to $Re_G = 10^5$, none of the scaling laws match the $n = 0$ predictions any longer. When the global Reynolds number reaches this value of 10^5, the scaling laws of the turbulent wake change to a non-equilibrium prediction which corresponds to either $n = 1$ or $n = 2$. In fact when looking at the results, a scaling law distinction can be made between trip sizes: $Re_G = 10^5 + T_1$ for which we seemingly have $n = 1$ and $Re_G = 10^5 + T_2$ for which it seems more accurate to use $n = 2$.

For the $Re_G = 10^5 + T_1$ flow, the mean flow scalings which best fit our data from $x/D = 7.0$ to $x/D = 40.1$ are $u_0/U_\infty \sim (x - x_0/D)^{-1}$ (see figure 3b) and $\delta/D \sim (x - x_0/D)^{1/2}$ (see figure 2b) in agreement with the $n = 1$ predictions. Not shown here, but the best power law fit to the centerline turbulent dissipation rate returns $\gamma \approx -2.5$ which is expected for $n = 1$. However, this power law fit is over the region $x/D = 19.5$ to $x/D = 40.1$, and it must be noted that $\gamma \approx -2.6$ can also fit these data comparably well over that region.

All in all, these results point towards $Re_G = 10^5 + T_1$ generating a spheroid turbulent wake which follows non-equilibrium scalings corresponding to $n = 1$. The validity of the dissipation exponent $n = 1$ is now directly examined by using the HWA and SPIV data to calculate C_ε, the SPIV data to calculate Re_δ and then checking the value of n in the power law relation $C_\varepsilon \sim (Re_G/Re_\delta)^n$. We have observed that that Re_δ and Re_λ decrease with increasing streamwise distance from the spheroid. In fact they decrease with increasing streamwise distance for all four wake configurations studied here. Incidentally, the values of Re_λ are significantly larger at all streamwise positions for $Re_G = 10^5$ than for $Re_G = 5.0 \cdot 10^4$ and $7.5 \cdot 10^4$, and they are consistently larger than 100 (except at the one or two furthest steamwise stations) only for $Re_G = 10^5$. C_ε is not as constant with x for $Re_G = 10^5$ as it is for $Re_G = 5.0 \cdot 10^4$ and $7.5 \cdot 10^4$. In figure 4b we performed the $C_\varepsilon \cdot Re_\delta$ multiplication to see its evolution streamwise, and $C_\varepsilon \cdot Re_\delta$ is observed to be globally constant.

The exponent $n = 1$ is a clear shift from $n = 0$ for the two lower values of Re_G and it coincides with the appearance at $Re_G = 10^5$ of a clear low-frequency peak in the turbulence power density spectra $E(St)$ ($St \equiv f/(U_x D)$ where f stands for frequency) at a distinguishable peak frequency $St_{peak} = 0.21$ (see figure 5), which suggests the presence of a large-scale coherent flow structure. No such evidence of large-scale coherent structure exists in the power spectra of the two wakes with lower values of Re_G where the data point to $n = 0$. This large-scale structure is also responsible for the higher values of Re_λ compared to the two lower global Reynolds numbers $Re_G = 5.0 \cdot 10^4$ and $Re_G = 7.5 \cdot 10^4$.

The low frequency peak in the spectra of the $Re_G = 10^5 + T_1$ wake is visible starting from $x/D = 13$ and reaches its highest energy values at $x/D = 16$ and $x/D = 19.5$. It remains well-defined further downstream even though global TKE levels decrease as we go downstream. It is remarkably close to a peak reported by Ortiz-Tarin *et al.* (2021) in their study of the same spheroid wake at the same Re_G value. Their peak value is $St = 0.28$ which they associated with a large helicoïdal structure.

The $Re_G \approx 10^5 + T_2$ wake is the same as the previous wake except that a trip step of size $T_2 = 0.6$ *mm* is used, which is double the size T_1. For this wake, the mean flow scalings which best fit our data from $x/D = 7.0$ to $x/D = 40.1$ are $u_0/U_\infty \sim (x - x_0/D)^{-1.2}$ (see figure 3c) and $\delta/D \sim (x - x_0/D)^{0.6}$ (see figure 2c) in agreement with the $n = 2$ predictions. The best power law fit to the centerline turbulent dissipation rate returns $\gamma \approx -2.6 = -13/5$ expected for $n = 2$, but this is very close to $\gamma \approx -5/2$ which corresponds to $n = 1$. Whether it is one or the other is not clear from our centerline HWA measurements alone both for the $Re_G = 10^5 + T_1$ and the $Re_G = 10^5 + T_2$ wakes.

Additional support for the dissipation exponent $n = 2$ in the case $Re_G = 10^5 + T_2$ is obtained by directly checking the value of n in the power law relation $C_\varepsilon \sim (Re_G/Re_\delta)^n$. The global trend $C_\varepsilon \cdot Re_\delta^2 \sim Const$ is only present in the $Re_G = 10^5 + T_2$ wake, see figure 4c. This is the only one of our four wakes which has the $n = 2$ non-equilibrium scalings previously seen in the simulations of Ortiz-Tarin *et al.* (2021).

Similarly to the $Re_G = 10^5 + T_1$ wake, a low frequency peak also appears in the turbulence power density spectra $E(St)$ of the $Re_G = 10^5 + T_2$ wake at a similar if not the same frequency $St_{peak} = 0.21$. This peak is broader in the spectra of the $Re_G = 10^5 + T_2$ wake than in the spectra of the $Re_G = 10^5 + T_1$ wake and is discernible starting from $x/D = 19.5$. As already mentioned, it suggests the presence of a large-scale coherent flow structure. As opposed to its counterpart in the $Re_G = 10^5 + T_1$ wake, it becomes less distinguishable as we go further downstream, and is arguably absent at $x/D = 40.1$. It is nevertheless remarkably close to the spectral peak reported by Ortiz-Tarin *et al.* (2021) who associated it to a large helicoïdal structure developping in the same region where we report $n = 2$ scalings experimentaly for the 6:1 spheroid turbulent wake.

In conclusion, we have observed centerline velocity deficit, wake hafl-width, and turbulent dissipation scalings with $n = 0$ for the $Re_G = 5.0 \cdot 10^4 + T_1$ and $Re_G = 5.0 \cdot 10^4 + T_1$ wakes, $n = 1$ for the $Re_G = 10^5 + T_1$ wake, and $n = 2$ for the $Re_G = 5.0 \cdot 10^4 + T_1$ wake. Three different scaling behaviours for four 6:1 spheroid wakes with same/similar levels of self-similarity, same 6:1 spheroid, same suspension system, same wind tunnel and same HWA and SPIV setup. The only differences are in the trip size, the global Reynolds number, the presence/absence of large-scale coherent flow structures and the local Reynolds numbers Re_λ.

CONCLUSIONS

The measurements that we performed at different high-Reynolds numbers in the wake of a 6:1 aspect ratio prolate spheroid with no angle of attack support the existence of three distinct sets of scaling laws depending on Reynolds number and boundary layer tripping size. The experiments were conducted in the LMFL laminar inflow long test section wind-tunnel under the same conditions for each flow case

With T_1 tripping size, the 6:1 prolate spheroid's turbulent wake is characterised by $n = 0$ equilibrium scalings when $Re_G = 5.0 \cdot 10^4$ and $Re_G = 7.5 \cdot 10^4$, $n = 1$ non-equilibrium scalings when $Re_G = 10^5$, but $n = 2$ non-equilibrium scalings when $Re_G = 10^5$ and the trip size is doubled from T_1 to T_2. This interpretation of our results is supported by the consistent dependence of the turbulence dissipation coefficient C_ε on the local Reynolds number.

The non-dimensional frequency of these structures is $St_{peak} = 0.21$, which is close to the value reported by Ortiz-Tarin *et al.* (2021) from their numerical simulations of the 6:1 prolate spheroid wakes at $Re_G = 10^5$.

ACKNOWLEDGEMENTS

This work was funded by the European Union (ERC, NoStaHo, 101054117). Views and opinions expressed are, however, those of the authors only and do not necessarily reflect those of the European Union or the European Research Council, Neither the European Union not the granting authority can be held responsible for them.

The equipment used in this work and operated by the platform PLEX (experimental platform for turbulence research) is funded under the project "Recherche et Innovation en Transports et Mobilité Eco-responsables et Autonomes" (RITMEA) CPER 2021-2027 (and previously CISIT then Elsat2020), co-funded by the European Regional Development Fund, the French state, the FEDER Hauts-de-France Regional Council and the recherche fondation FR TTM CNRS 3733.

REFERENCES

Cafiero, G., Obligado, M. & Vassilicos, J.C. 2020 Length scales in turbulent free shear flows. *Journal of Turbulence* **21** (4), 243–257.

Coudert, Sebastien J M & Schon, Jean-Paul 2001 Back-projection algorithm with misalignment corrections for 2D3C stereoscopic PIV. *Meas. Sci. Technol.* **12** (9), 1371–1381.

Dairay, T., Obligado, M. & Vassilicos, J. C. 2015 Non-equilibrium scaling laws in axisymmetric turbulent wakes. *J. Fluid Mech.* **781**, 166–195.

Dairay, T. & Vassilicos, J.C. 2016 Direct numerical simulation of a turbulent wake: The non-equilibrium dissipation law. *International Journal of Heat and Fluid Flow* **62**, 68–74.

Foucaut, J M, Coudert, S, Braud, C & Velte, C 2014 Influence of light sheet separation on SPIV measurement in a large field spanwise plane. *Meas. Sci. Technol.* **25** (3), 035304.

Lecordier, B. & Trinité, M. 2004 Advanced PIV algorithms with Image Distortion Validation and Comparison using Synthetic Images of Turbulent Flow. In *Particle Image Velocimetry: Recent Improvements* (ed. M. Stanislas, J. Westerweel & J. Kompenhans), pp. 115–132. Berlin, Heidelberg: Springer Berlin Heidelberg.

Ortiz-Tarin, J.L., Nidhan, S. & Sarkar, S. 2021 High-Reynolds-number wake of a slender body. *J. Fluid Mech.* **918**, A30.

Pope, Stephen B. 2000 *Turbulent flows*, 1st edn. Cambridge: Cambridge Univ. Press.

Scarano, F 2002 Iterative image deformation methods in PIV. *Meas. Sci. Technol.* **13** (1), R1–R19.

Soloff, S M, Adrian, R J & Liu, Z-C 1997 Distortion compensation for generalized stereoscopic particle image velocimetry. *Meas. Sci. Technol.* **8** (12), 1441–1454.

Soria, Julio 1996 An investigation of the near wake of a circular cylinder using a video-based digital cross-correlation particle image velocimetry technique. *Experimental Thermal and Fluid Science* **12** (2), 221–233.

Taylor, G. I. 1938 The Spectrum of Turbulence. *Proc. R. Soc. Lond. A* **164** (919), 476–490.

Townsend, A. A. 1976 *The structure of turbulent shear flow*, 2nd edn. Cambridge [Eng.] ; New York: Cambridge University Press.

Vassilicos, J. Christos 2015 Dissipation in Turbulent Flows. *Annu. Rev. Fluid Mech.* **47** (1), 95–114.

Welch, P. 1967 The use of fast Fourier transform for the estimation of power spectra: A method based on time averaging over short, modified periodograms. *IEEE Trans. Audio Electroacoust.* **15** (2), 70–73.

Wieneke, B. 2005 Stereo-PIV using self-calibration on particle images. *Exp Fluids* **39** (2), 267–280.

Willert, C. E. & Gharib, M. 1991 Digital particle image velocimetry. *Experiments in Fluids* **10** (4), 181–193.